applied sciences

MDPI

Article

Synthesis and Characterization of Anatase TiO_2 Nanorods: Insights from Nanorods' Formation and Self-Assembly

Seyed Naveed Hosseini, Xiaodan Chen, Patrick J. Baesjou *, Arnout Imhof * and Alfons van Blaaderen *

Soft Condensed Matter, Debye Institute for Nanomaterials Science, Utrecht University, Princetonplein 1, 3584 CC Utrecht, The Netherlands; n.hosseini@uu.nl (S.N.H.); x.chen1@uu.nl (X.C.)
* Correspondence: p.j.baesjou@uu.nl (P.J.B.); a.imhof@uu.nl (A.I.); a.vanblaaderen@uu.nl (A.v.B.)

Abstract: Highly crystalline, organic-solvent-dispersible titanium dioxide (TiO_2) nanorods (NRs) present promising chemicophysical properties in many diverse applications. In this paper, based on a modified procedure from literature, TiO_2 NRs were synthesized via a ligand-assisted nonhydrolytic sol-gel route using oleic acid as the solvent, reagent, and ligand and titanium (IV) isopropoxide as the titanium precursor. This procedure produced monodisperse TiO_2 NRs, as well as some semi-spherical titania nanocrystals (NCs) that could be removed by size-selective precipitation. X-ray diffraction and selected area electron diffraction results showed that the nanorods were anatase, while the semipheres also contained the TiO_2(B) phase. By taking samples during the particle growth, it was found that the average length of the initially grown NRs decreased during the synthesis. Possible reasons for this unusual growth path, partially based on high-resolution transmission electron microscopy (HRTEM) observations during the growth, were discussed. The dispersion of anatase TiO_2 nanorods was capable of spontaneous formation of lyotropic liquid crystals on the TEM grid and in bulk. Considering high colloidal stability together with the large optical birefringence displayed by these high refractive index liquid crystalline domains, we believe these TiO_2 NRs dispersions are promising candidates for application in transparent and switchable optics.

Keywords: titanium dioxide; nanorods; self-assembly; inorganic liquid crystals

check for updates

Citation: Hosseini, S.N.; Chen, X.; Baesjou, P.J.; Imhof, A.; van Blaaderen, A. Synthesis and Characterization of Anatase TiO_2 Nanorods: Insights from Nanorods' Formation and Self-Assembly. *Appl. Sci.* **2022**, *12*, 1614. https://doi.org/10.3390/app12031614

Academic Editor: Francesco Tornabene

Received: 21 December 2021
Accepted: 27 January 2022
Published: 3 February 2022

Publisher's Note: MDPI stays neutral with regard to jurisdictional claims in published maps and institutional affiliations.

Copyright: © 2022 by the authors. Licensee MDPI, Basel, Switzerland. This article is an open access article distributed under the terms and conditions of the Creative Commons Attribution (CC BY) license (https://creativecommons.org/licenses/by/4.0/).

1. Introduction

Nanocrystalline TiO_2 has been receiving increasing attention in many applications such as optoelectronics [1], catalysis and photocatalysis (such as water splitting, air, and water purification) [2–8], solar energy conversion [9], gas sensing [10], and nanostructured coatings for biomedical implants due to its modified material properties and chemical reactivity at the nanoscale [11]. The literature on producing nanocrystalline titania is quite extensive, leading to TiO_2 nanoparticles (NPs) in various sizes, morphologies, and crystalline phases in different yield scales [7,12]. Therefore, choosing an appropriate method to synthesize titania NPs consistent with the desired characteristics for the final application is of great importance. Among titania polymorphs that are commonly recognized, rutile is known to be thermodynamically the most stable phase for bulk material at standard pressure (1 bar) within the range 300–1000° K [13]. However, anatase and the less common brookite and titanium dioxide bronze phase (TiO_2(B)), are also formed commonly at the nanoscale [14,15]. Though brookite and TiO_2(B) are rarely observed in nature, their importance in photocatalysis, photovoltaics, and lithium-ion insertion has been recently recognized [16]. The transformation sequence among anatase, brookite, and rutile is size-dependent and their transformation into each other can be reversed even by slight differences in the surface energies [8]. In the case of TiO_2(B), it can be nucleated directly from the solution as a metastable phase and tends to transform into anatase titania at temperatures above 800° K [17].

We are interested in the unique intrinsic properties of crystalline titania NPs, such as high refractive indexes, wide bandgap, and strong UV absorption with no light absorption

in the visible part of the spectrum. Additionally, we want to benefit from the shape and orientation-dependent collective properties of these inorganic NPs in liquid crystalline states for optical applications, as such nanorod (NR) liquid crystal phases can be switched at lower field strengths than molecular counterparts [18,19]. Thus, we focused on titania NRs as colloidal anisotropic building blocks to not only benefit from their spontaneous liquid crystal (LC) formation but also to gain other advantages over spherical titania counterparts in terms of high surface-to-volume ratio, improved number of delocalized carriers, and enhanced charge transport provided by their anisotropic geometry for relevant research in optoelectronics and photocatalysis [20,21]. To achieve crystalline titania NRs, solution-phase methods, and in particular non-hydrolytic sol-gel techniques, are well known to give precise control over particle size, shape, and polymorphic phases by employing structure-directing agents, i.e., ligand organic molecules. Furthermore, these ligand molecules offer general dispersibility in diverse organic solvents [22]. Therefore, preparation of concentrated dispersions of titania NRs is achievable, which is important for lyotropic liquid crystal formation [23,24]. Many reports by different research groups such as Colvin et al. [25], Moritz et al. [26], Alivisatos et al. [27], Niederberger et al. [28], Vioux et al. [29,30], Han et al. [31], Cozzoli et al. [20,32,33], Murray et al. [3,5,22], and Hyeon et al. [34,35] have been devoted to the optimizing and understanding of titania NRs synthesis via non-hydrolytic sol-gel methods. In all of those experiments, the TiO_2 NRs are formed via hydrolysis and condensation reactions. In these reactions, the oxygen for the oxide NPs formation is provided by the solvent (ethers, alcohols, ketones, or aldehydes) or by the organic constituent of the precursor (alkoxides or acetylacetonates) [30,36]. Along with that, several key condensation reactions are proposed depending on the precursor and solvent in the reaction system such as alkyl halide elimination by a titanium alkoxide and a titanium halide reaction [27,29,35], ester elimination between titanium carboxylates and titanium alkoxides reaction [30,34], and ether elimination by two titanium alkoxides reaction [37].

Herein we report a synthesis route, based on a modified procedure from the literature [34], to produce titanium dioxide NRs from ultrathin NRs via a ligand-assisted nonhydrolytic sol-gel pathway in which the ligands (oleic acid, OLAC) also acted as the solvent and reagent. The used synthetic procedure also produced semispherical nanocrystals (NCs), but these could be removed from the NRs by size-selective precipitation. A possible formation mechanism for the ultrathin NRs, morphological evolution, and accompanying NCs is discussed as it was observed that the initial nanorod length was seen to decrease after the first 10 min of synthesis. Moreover, we showed that the anatase NRs we obtained were monodisperse enough to spontaneously self-organize into inorganic smectic liquid crystal phases on the TEM grid and in bulk, making them a promising candidate for LC-based optoelectronic applications.

2. Materials and Methods

2.1. Materials

Titanium (IV) isopropoxide or TTIP ($Ti(OCH(CH_3)_2)_4$, 97.0%), oleic acid (OLAC, 90%), acetone, and toluene were purchased from Sigma Aldrich (Amsterdam, the Netherlands) and used as received. All experimental procedures were carried out either in an inert atmosphere using a standard Schlenk line setup or in a glove box.

2.2. The Modified Synthesis of TiO_2 NRs

Anatase titanium dioxide NRs were synthesized following a slightly modified version of the synthesis described in the literature by Joo et al. [34] Our modifications were mainly related to the following factors: (I) we reduced the precursor amounts by half, (II) lowered the reaction temperature from 270 °C to 250 °C, and (III) performed a careful size-selective washing step, as discussed below. In a typical synthesis, OLAC (100.0 mmol, 31.6 mL) was degassed in a 250 mL three-neck round bottom flask at 120 °C for an hour under vacuum and vigorous stirring. Then the flask was cooled down under vacuum to 40 °C, followed by switching to nitrogen and the swift addition of TTIP (34.0 mmol, 10 mL) which

was prepared in the glove box in advance. The mixture was then heated up to 250 °C in 20 min and kept at this temperature for 2 h. Caution should be taken as the reaction is rather violent with the concomitant release of gases and foam formation expanding in the flask and should be controlled by nitrogen overflow/pressure. After thermal fluctuations at high temperatures, the yellow solution gradually turned into a white-gray foam and finally a gray solution. The heating mantle was then removed after 2 h and the flask was allowed to cool to room temperature. To effectively separate TiO_2 NRs specifically in terms of their length with the desired polydispersity index (standard deviation divided by mean length), a size-selective precipitation process was performed on as-synthesized TiO_2 NCs. We observed that to achieve a higher yield of NRs, it was crucial to separate larger NCs (here TiO_2 NRs) from the reaction mixture *just through centrifugation prior to the addition of antisolvent in the size-selective precipitation process*. Therefore, at first, we centrifuged the crude reaction mixture at 6000 rcf for 10 min and extracted the supernatant. In the next step, we separated the TiO_2 NRs that were redispersed in toluene by the addition of acetone dropwise as an antisolvent to the NRs dispersion. The milky solution was centrifuged at 3400 rcf for 5 min and then NRs precipitations were redispersed in toluene. The washing step was repeated at least two times to achieve optically clear dispersions of titania NRs. The titania NRs were relatively monodisperse in their length (σ_L = 14%). The dimension of the NRs was on average 3.6 ± 0.3 nm (diameter) and 24.6 ± 3.4 nm (length) while the semispherical NCs had an average diameter of 5.7 nm. The NCs were redispersible in a variety of nonpolar solvents such as toluene or hexane. However, we chose toluene as a solvent in purification steps since it has a high refractive index which reduces the van der Waals attractions between the rods and is also a good solvent for OLAC. It has been shown that hexane has a higher solubility for oleic acid than toluene and can strip off ligands in the presence of antisolvent, while in toluene ligands remain at the surface of the NPs [38]. To monitor the evolution of the TiO_2 NCs, we extracted aliquots of the hot reaction mixture at scheduled time intervals using long capillary soda-lime glass Pasteur pipettes. These hot extractions were swiftly cooled down to room temperature via quenching in a toluene medium to stop further crystal growth and investigated by the transmission electron microscopy technique.

2.3. Self-Assembly of TiO_2 NRs

Typically, a droplet (~5 µL) of ligand-capped titania NRs dispersion with a low concentration (roughly 4 mg/mL) was dropcast on a carbon-coated 300 mesh copper TEM grids (Agar Scientific). The TEM grids were further dried in a vacuum chamber to remove residuals and used for microscopy analysis. To examine liquid crystalline structures of self-assembled domains in bulk, a sedimentation experiment was performed as previously reported elsewhere [18,39]. Briefly, a glass capillary (0.1 × 1.0 × 60.0 mm^3, Vitrocom) was filled with ligand-capped titania NRs dispersion with an initial volume fraction of 29.8 vol.%, effective length L = 27.6 nm, diameter D = 6.6 nm, and an aspect ratio of 4.18, in which the ligand length of 1.5 nm was taken into account. Then, the capillary was sealed using a two-component epoxy glue (Bison Kombi rapid), left vertically to sediment for 10 days, and was further investigated by polarizing optical microscopy (POM) technique.

2.4. Characterization of TiO_2 NCs

The X-ray diffraction analysis (XRD) was performed using a Bruker-AXS D2 Phaser X-ray diffractometer with Co Kα radiation (λ = 1.79026 Å) operated at 30 kV and 10 mA. Transmission electron microscopy and selected area electron diffraction (SAED) of the brookite NRs were performed on an FEI Tecnai 20 electron microscope operating at 200 kV. The crystalline structures of the TiO_2 NRs were measured by a high-resolution transmission electron microscope (FEI-Talos F200X electron microscope). Typically, at least 100 particles were counted to calculate the anatase NRs size distribution and polydispersity index. The bandgap of the NRs was studied at room temperature (20 °C) with a diffuse reflectance UV-Vis spectrometer (HP 8452a model). Typically, the NRs dispersion was diluted in

toluene and added to a quartz cuvette (optical path: 10 mm) sealed with a Teflon stopper. The absorption spectrum was measured while the wavelength was varied from 250 nm to 700 nm. For POM images, a Leica DM2700P microscope equipped with crossed polarizers a Nikon Z6 camera was utilized.

3. Results and Discussions

3.1. Growth Mechanism of TiO_2 Nanocrystals

Titanium dioxide nanocrystals (NCs) were synthesized following a slightly modified synthesis method as described by Joo et al. [34] where oleic acid (OLAC) was used as the solvent, reagent, and ligand [40]. Our modifications were mainly related to the reduced precursor amounts and lowering the reaction temperature from 270 °C to 250 °C to control the reaction temperature fluctuations and foam expansions. Figure 1 shows the as-synthesized TiO_2 NCs characterized by TEM and high-resolution TEM (HRTEM) images. As can be seen in Figure 1a, as-synthesized TiO_2 NCs mostly consisted of nanorods (NRs) with various lengths as well as some semispherical NCs. To effectively separate the TiO_2 NRs specifically in terms of their length to obtain the desired polydispersity index (standard deviation divided by mean length), size-selective precipitation, or more correctly aggregation, was performed on the TiO_2 mixture. This well-known purification technique is mainly based on the magnitude of the van der Waals attraction forces between particles which increase with particle size [41]. In the case of NRs, the van der Waals attraction forces induced the aggregation between NRs with larger lengths [42]. We found that to achieve a higher yield of monodisperse NRs (yield of ~50% or almost 1 g of NRs), it was crucial to separate first the larger NCs (here TiO_2 NRs) from the reaction mixture *just through centrifugation* prior to the addition of antisolvent in the size-selective precipitation process. After centrifugation of the reaction mixture, separation of the TiO_2 NRs by length was highly efficient by the dropwise addition of acetone as an antisolvent to the dispersion of the NRs in toluene. Due to the hydrophobicity of the ligand layer around TiO_2 NRs, the dispersion of the NRs was destabilized by the addition of the polar acetone which resulted in the aggregation and fast sedimentation of the NRs leaving many of the synthetic by-products and shorter rods in solution. Finally, both the TiO_2 NRs as main products and the semispherical NCs left in the supernatant were redispersible in a variety of nonpolar solvents such as toluene as shown in Figure 1d,e and resulted in the isolation of relatively monodisperse TiO_2 NRs (σ_L = 14%). The dimension of the NRs was on average 3.6 ± 0.4 nm (thickness) and 24.6 ± 3.4 nm (length), while the semispherical NCs had an average diameter of 5.7 nm.

Figure 1b shows the selected area electron diffraction (SAED) pattern of these NRs revealing the highly crystalline anatase phase. The reflected rings were clearly indexed to (101), (103), (004), (200), and (105) planes of anatase indicating the high crystallinity of these particles which is consistent with the HRTEM images and X-ray diffraction (XRD) results in Figure 4. In Figure 1c where a (010) zone axis is perpendicular to the imaging plane, a single nanorod can be seen to have grown along its *c* axis in the (001) direction. The reason is that (001) surfaces in the anatase phase have a higher surface energy in comparison to (101) surfaces [26,43]. Thus, the typical fast growth in anisotropic anatase NRs is observed with a preferential growth in the (001) direction as was also the case in our synthesis. The lattice fringes of approximately 0.35 nm are depicted with yellow parallel lines corresponding to the (101) planes of the anatase phase.

In the following, we will discuss the mechanism of the titania NRs formation in our experiment based on the literature on the nonhydrolytic sol-gel routes to synthesize titanium oxide NPs [27,31,34,44–47] and on what we observed by following our synthesis in time by taking samples of reaction mixtures at 10-min intervals.

In general, nonhydrolytic sol-gel processes can be divided into two main categories: ligand-assisted and solvent-controlled routes. In the case of the ligand-assisted process, ligands, mainly in the form of hot ligand solutions (e.g., trioctylphosphine oxide, oleic acid, and oleylamine), are present in the reaction mixture, either as a solvent or as a coordinating ligand providing control over the growth, size, and shape of the metal oxide NPs [46].

However, in solvent-controlled approaches, the initial reaction mixture mainly consists of two components, metal oxide precursors and common organic solvents. Thus the role of solvents may include acting as a reactant, oxygen donor, structure-directing agent, or reducing factor [28,48]. One should also keep in mind that these nonhydrolytic sol-gel routes, also known as nonaqueous reactions, are not necessarily totally water-free. In fact, even though the initial components of the reaction mixture have been dried and degassed, specific organic reactions are able to produce water in situ (e.g., aldol condensation and esterification reactions), rendering the system in principle hydrolytic. Therefore, even in the (virtual) absence of water, it is possible to have hydroxylation reactions [36].

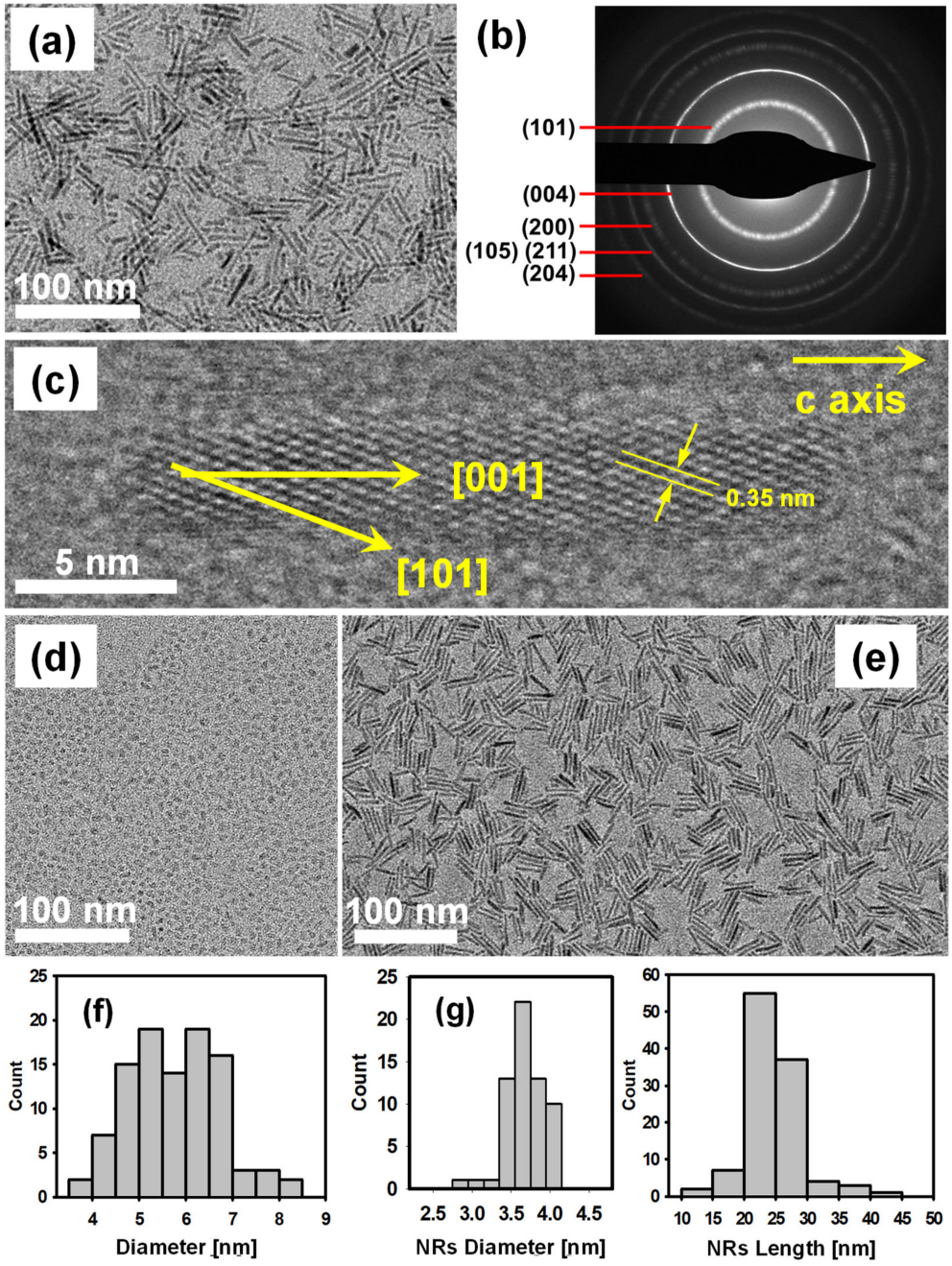

Figure 1. (**a**) As-synthesized TiO_2 NCs including NRs of different aspect ratios and semispherical NCs; (**b**) SAED pattern of anatase NRs presenting reflected rings clearly indexed to typical planes of anatase; (**c**) an individual anatase NR that has a (010) zone axis growing along the (001) direction. (**d**–**g**) TiO_2 NCs after the size-selective process in two main categories, NRs and semispherical NCs, and their corresponding size distributions from a statistical analysis of TEM images.

In our experiment, titania NRs were synthesized via a ligand-assisted nonhydrolytic sol-gel method in which the rapid thermal decomposition of a titanium precursor (titanium (IV) isopropoxide or TTIP) occurred in a hot solvent solution (OLAC), at a relatively high temperature (around 250 °C). It is well-known that titanium alkoxides are relatively reactive (e.g., as compared to silicon alkoxides) and almost instantly react with carboxylic acids (e.g., oleic acid, decanoic acid, linoleic acid, etc.,) even under mild conditions producing mixed alkoxy carboxylates and hydroxyalkoxides [20,40,49]. For instance, it was shown that titanium (IV) butoxide ($Ti(OBu)_4$ where Bu refers to $-C_4H_9$) can readily react with linoleic acid ($C_{17}H_{31}CO_2H$) yielding a titanium butoxide-carboxylate complex $Ti(OBu)_{4-x}(C_{17}H_{31}CO_2)_x$ with the release of *x*BuOH. This BuOH formed, may react with unreacted linoleic acid left in the mixture leading to the formation of water by an esterification reaction [46,49]. Analogous to the literature, we believe that in our experiment, upon the addition of TTIP ($Ti(O^iPr)_4$ where Pr refers to $-C_3H_7$) to the degassed OLAC ($C_{17}H_{33}COOH$) solution at room temperature and as indicated by a color change of the mixture to pale yellow, a titanium carboxylate complex ($(C_{17}H_{33}COO)_x-Ti(O^iPr)_{4-x}$) formed with the release of *x*PrOH. Since the OLAC molecules were present in an excess amount acting as both ligand and solvent, therefore *x*PrOH could react with OLAC molecules and release water molecules via an esterification reaction. The water produced could then react with the titanium carboxylate complex to generate Ti−OH and subsequently through a hydrolysis–condensation process, **Ti**−**O**−**Ti** bonds were formed [50]. It has been shown that in synthetic routes where the ligand and solvent are the same, the desorption rate of ligand bound at the surface of the NCs is low giving them higher colloidal stability [47].

It has also been demonstrated that the in situ water generated during the esterification reaction favors the formation of anatase and TiO_2(B) which is in agreement with our results in Figure 4, as well [51]. The abovementioned reaction route is described in Equations (1)–(3):

$$Ti\left(O^iPr\right)_4 + xC_{17}H_{33}COOH \rightarrow (C_{17}H_{33}COO)_x - Ti\left(O^iPr\right)_{4-x} + xPrOH \quad (1)$$

$$PrOH + C_{17}H_{33}COOH \rightarrow C_{17}H_{33}COOPr + H_2O \quad (2)$$

$$\begin{aligned}(C_{17}H_{33}COO)_x - Ti\left(O^iPr\right)_{4-x} + H_2O &\rightarrow (C_{17}H_{33}COO)_x\left(O^iPr\right)_{3-x}TiOH + xPrOH\\ (C_{17}H_{33}COO)_x\left(O^iPr\right)_{3-x}TiOH + (C_{17}H_{33}COO)_x\left(O^iPr\right)_{3-x}TiOH &\\ \rightarrow (C_{17}H_{33}COO)_x\left(O^iPr\right)_{3-x}\mathbf{Ti}-\mathbf{O}-\mathbf{Ti}(C_{17}H_{33}COO)_x\left(O^iPr\right)_{3-x} + H_2O &\end{aligned} \quad (3)$$

Although we think that the hydrolysis followed by condensation is the main route of oxide formation, the possibility of a nonhydrolytic condensation of titanium carboxylate complex to form **Ti**−**O**−**Ti** bonds cannot be ruled out, either [20]. It is known that an oxo bridge can be formed by a condensation reaction between two functional groups bonded to two metal centers (here titanium atoms) along with eliminating an organic ester molecule [46]. Thus, after the formation of the titanium carboxylate complex, also a transesterification can occur between the complex and TTIP precursor to generate the **Ti**−**O**−**Ti** bonds and eliminate an ester. These reaction steps are shown in Equations (4) and (5):

$$Ti\left(O^iPr\right)_4 + (C_{17}H_{33}COO)_x - Ti\left(O^iPr\right)_{4-x} \rightarrow (C_{17}H_{33}COO)_{x-1}\left(O^iPr\right)_{4-x}\mathbf{Ti}-\mathbf{O}-\mathbf{Ti}\left(O^iPr\right)_3 + (C_{17}H_{33}COOPr) \quad (4)$$

$$n(C_{17}H_{33}COO)_x - Ti\left(O^iPr\right)_{4-x} \rightarrow {}^n/_2\left[\left(O^iPr\right)_{3-x}\mathbf{Ti}-\mathbf{O}-\mathbf{Ti}(C_{17}H_{33}COOPr)_{x-1}\right] + {}^n/_2\,(C_{17}H_{33}COOPr) \quad (5)$$

Cozzoli et al. suggested that these molecular species were enclosing a compact **Ti**−**O**−**Ti** framework of hexa-coordinated Ti atoms and could be regarded as titania

monomers protected by carboxylate ligands. In these monomers, OLAC molecules have a tendency to bridge titanium centers [20]. Therefore, we surmise that titania NCs synthesized in our experiment might have been formed via both hydrolytic–condensation and nonhydrolytic–condensation routes, but it is not clear to what extent each path contributed.

In Figure 2, we monitored the progressive evolution of TiO_2 NCs by extracting aliquots of the hot reaction mixture at scheduled time intervals. These hot extractions were swiftly cooled down to room temperature via quenching in toluene to stop further crystal growth. Interestingly, ultrathin TiO_2 NRs (1.8 ± 0.3 nm (thickness) and 36.4 ± 10.1 nm (length)) were produced in the early stages of the reaction (first 10 min). These ultrathin NRs were of the anatase polymorph. This relatively fast formation of the titania NRs was also reported in the literature for the case of $Ti(OBu)_4$ decomposed in a pure OLAC medium leading to anatase NRs in less than 15 min [47]. In each panel of Figure 2, the length distribution of TiO_2 is shown as a histogram. In addition to the length distributions, we can observe that the ultrathin TiO_2 NRs became thicker over time from 1.8 ± 0.3 nm to 3.6 ± 0.4 nm. Moreover, in the first 10 min of the experiment, ultrathin NRs had a broad length distribution of 36.4 ± 10.1 nm. After 10 more minutes, shorter but thicker NRs of 21.8 ± 2.8 nm were mostly detected in the reaction mixture, which then increased in both thickness and length, finally resulting in nanorods with a broad length distribution of 27.6 ± 6.9 nm and a collection of semispherical NCs. We also noticed that during the growth steps, some NRs became unequally thicker such that the thickness was somewhat larger in either one tip of the NRs (matchstick-like NR shown in Figure 2b-inset) or in both tips (dumbbell-like NR shown in Figure 2d-inset).

For titania NRs, a process of shape evolution after initial crystallization has been described in several previous reports, as well [26,27,43,49,52,53]. In some cases, anatase NCs that were formed in acidic conditions nucleated almost exclusively as truncated tetragonal bipyramidal NCs with (101), (001), and (010) facets [22,54]. Then, these primary NCs were kinetically promoted to grow via the oriented attachment mechanism [55,56]. We note that oriented attachment in one, two, three dimensions as well as mesocrystal formation have been reported frequently for surface-functionalized titania NPs synthesized in both hydrolytic and nonhydrolytic media [26,55,57]. Elaborate investigations by Dalmaschio and Leite [47] on anatase NRs, synthesized by thermal decomposition of titanium(IV) butoxide in an OLAC mixture revealed that the oriented attachment of these truncated tetragonal bipyramidal NCs occurs via sharing the (001) plane with a preferential growth in the (001) direction. In our results, we also observe typical morphological evolution as a function of time, for instance, an increase in the thickness of the NRs while the length reduced in the NRs and the emergence of relatively smaller NRs and NCs. Dalmaschio and Leite attributed these shape alterations to the fragmentation of the titania NRs into smaller NCs induced by a Rayleigh instability-like phenomenon [36,47]. Furthermore, they stated that the mass transportation to the tips of the NRs via a surface diffusion process could kinetically advance the detachment process. In the Rayleigh instability phenomenon, an unstable liquid cylinder breaks into droplets driven by surface tension fluctuations coupled with a lowering of the total energy. It has been proposed that under certain circumstances, this concept can be extended to solid NPs and therefore NRs could also be vulnerable to fragmentation into smaller NPs [58–61].

Although we cannot rule out the occurrence of directed attachment during the growth steps, we believe that due to the existence of ligands in the solution, the growth mechanism in Figure 2 is mainly attributed to the fast out-of-equilibrium growth of the NRs from the solution.

In Figure 3, HRTEM images of several synthesized anatase NRs have been presented. As can be observed, the structural features depicted by yellow arrows and lines on the surface of the NRs such as steps, corrugated sides, zigzag patterns, and sharp edges give indications of the critical pinch points formed during the surface diffusion step that are vulnerable to the detachment. Considering TEM images of ultrathin NRs formed in the early stages of the reaction (Figure 2) and HRTEM images of final NRs in Figure 3, the

Rayleigh instability-like detachment phenomena could also be the reason in our experiment that led to shorter titania NRs and pinched off semispherical titania NCs. However, further in-depth investigations are needed to precisely confirm the exact mechanism behind these TiO_2 NRs growth and their shape evolution during this experiment.

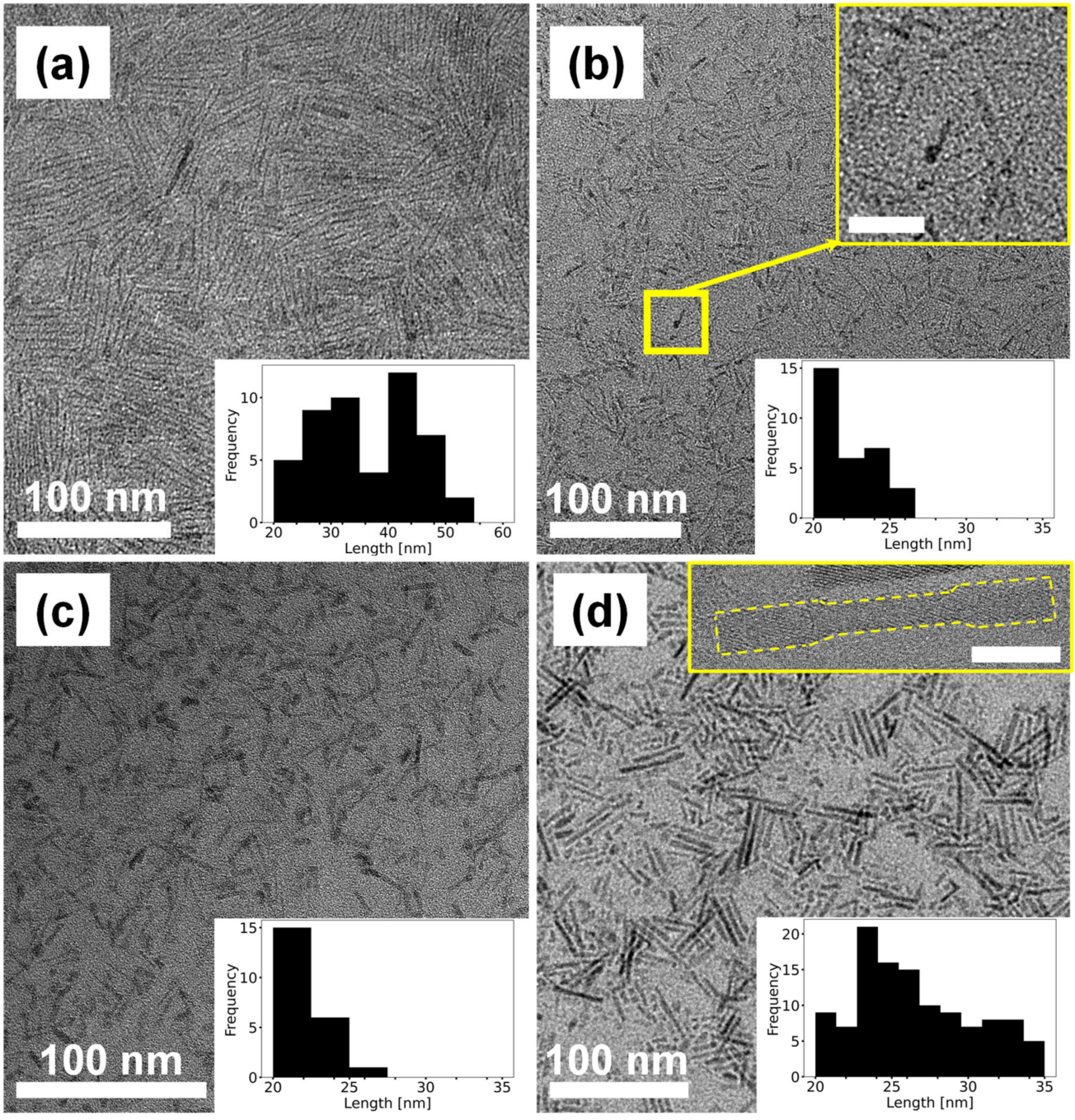

Figure 2. (**a**–**d**) TEM micrographs of TiO_2 NCs depicting progressive evolution of NCs at different time intervals (10 min, 20 min, 60 min, and 120 min, respectively) from ultrathin NRs to the final mixture of NRs of various lengths and semispherical NCs. The length distributions of TiO_2 are shown in histograms as insets with black columns. The average thickness of the NRs are 1.8 ± 0.3 nm in (**a**), 2.6 ± 0.5 nm in (**b**), 2.9 ± 0.7 nm in (**c**), and 3.6 ± 0.4 nm in (**d**). Inset in (**b**) shows the occurrence of irregularities at the tip of the NRs. Inset in (**d**) shows an HRTEM image of a single NR exhibiting a dumbbell shape at higher resolutions. Scale bar in b-inset is 25 nm and in d-inset is 5 nm.

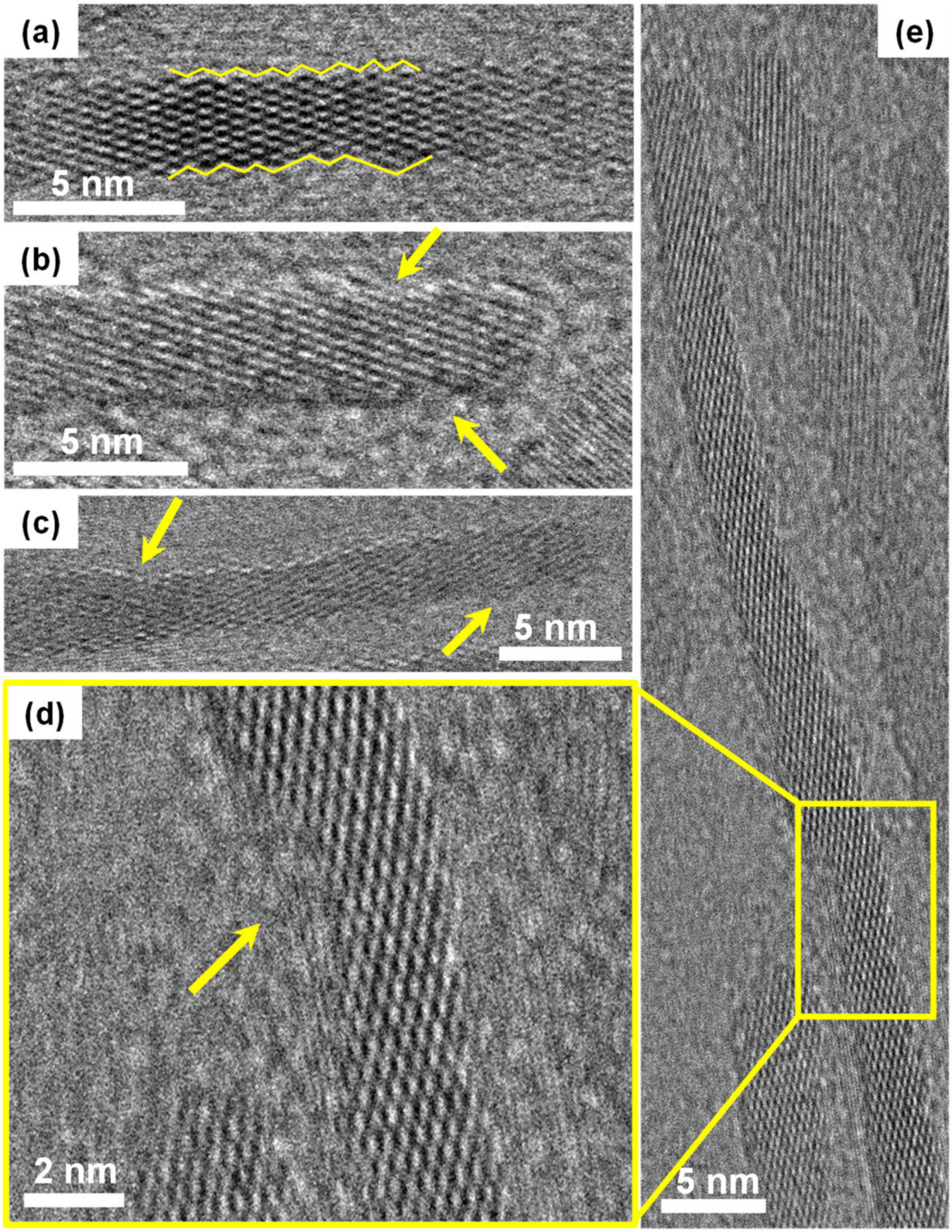

Figure 3. HRTEM micrographs of anatase NRs. (**a**–**e**) Surface features labeled by yellow arrows and lines on the surface of the NRs such as steps, corrugated sides, zigzag patterns, and sharp edges demonstrating give indications of the critical pinch points vulnerable to the detachment.

3.2. Characterization of Synthesized TiO_2 Nanocrystals

The crystallinity of the synthesized NCs was analyzed by the XRD technique (next to HRTEM observations and selected area electron diffraction results). Contrary to the results presented in the paper from which we follow the synthesis protocol (Joo et al. [34]) our XRD patterns (Figure 4) confirmed the existence of two titanium oxide polymorphs in the resulting NCs. Both the anatase phase and the titanium dioxide bronze phase (TiO_2(B)) could be recognized in our data. The XRD data, together with reference data of anatase TiO_2 (JCPDS-01-086-1155) and TiO_2(B) (JCPDS-00-046-1238), respectively, are shown in Figure 4, as well. In the case of anatase NRs, the relative intensity of the diffraction peak for (004) planes has been reported to become more pronounced as compared to the intensity of (200) planes [31,62]. This is a well-known phenomenon for anatase crystals if their anisotropic growth occurs along the *c* axis of the anatase lattice: the (004) diffraction peaks become stronger and sharper in comparison to (200) diffraction peaks and this is consistent with our TEM observations and the NRs SAED pattern in Figure 1b [26,34,49,63]. Furthermore, the bandgap of the anatase NRs was found to be ca. 3.28 eV by using their light absorption spectrum. The measured bandgap value was indeed analogous to reported optical bandgaps for nanocrystalline anatase NPs [5,34,64] (See Figure S1). To confirm that the peak broadening arose from NCs' size and shape effects, the average crystallite sizes of the anatase NCs were calculated by using the Scherrer formula [65] (See Table S1). Scherrer analysis from the (101), (200), and (004) diffraction peaks yields approximately 3.8, 3.5, and 19.9 nm, respectively, for the dimensions of the anatase NRs which are in agreement with the measured width and length from the TEM micrographs. Furthermore, the optical properties of the anatase NRs were characterized using their light absorption spectrum. Even though several diffraction peaks could be matched with the anatase reference signal, some other peaks at 34.4°, 35.4°, 36.2°, and 52.3° were pointing at the existence of another phase. Dickerson et al. suggested that these peaks could correspond to crystalline OLAC aggregated present among the TiO_2 NRs due to the fact that these NRs were formed in an excess amount of OLAC [66]. However, in our experiment, TiO_2 NRs were purified via a size-selective aggregation process after the synthesis step, therefore the presence of aggregated OLAC seems less likely to us. Moreover, a possible explanation of these signals could be the formation of brookite titania as an impurity, as it has been reported before during the synthesis of the other polymorphs [25,63,67]. Although the diffraction peak located at 36.2° could be assigned to the (121) plane of the brookite phase, the other three diffraction peaks at 34.4°, 35.4°, and 52.3° are not compatible with the brookite, anatase, or rutile polymorphs [68]. After careful examination, we concluded that the last four measured reflections could be a fit for the TiO_2(B) phase of titania, which is given in the reference card (JCPDS-00-046-1238). The (001), (−111), (003) reflections are typical of TiO_2(B) titania which were detected in the XRD patterns of both the NRs and the semispherical NCs [17,69]. These peaks are relatively more prevalent in the semispherical NCs rather than NRs. The reason could be the existence of semispherical NCs left after the size-selective process among anatase NRs since the full separation of the small NCs from bigger NRs is practically difficult. Furthermore, it has been shown that surface hydroxylation during TiO_2(B) NCs formation will introduce surface relaxation and thereby the TiO_2(B) NCs may exhibit an ellipsoidal shape in the c direction [17,69]. Therefore, not only the semispherical NCs, found mostly in the supernatant, but also some of the shorter NRs left among anatase NRs after the purification step could be elongated TiO_2(B) NCs.

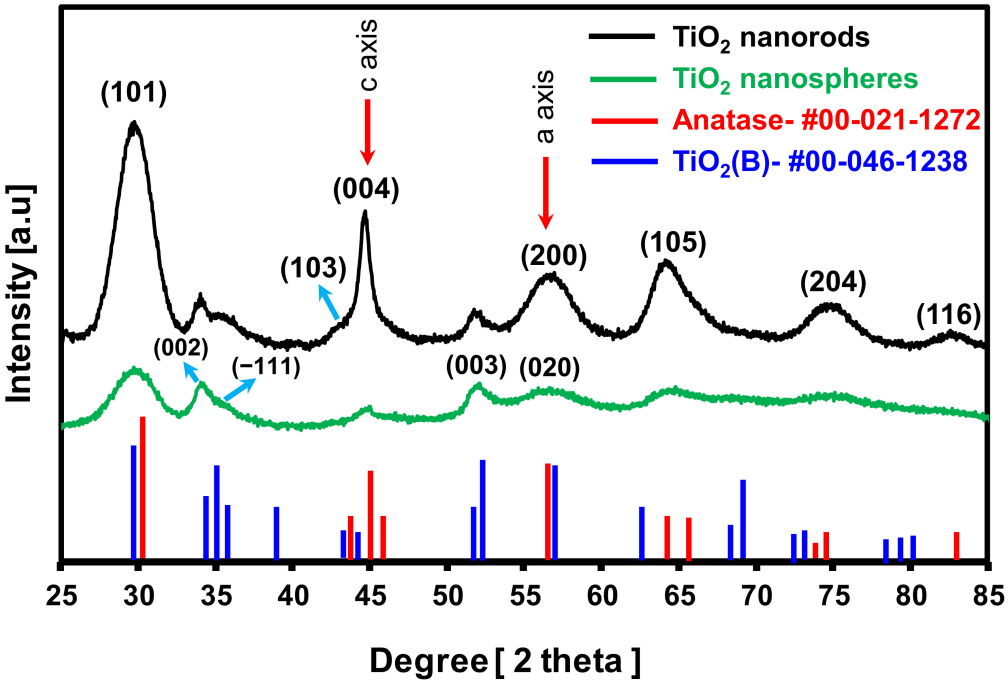

Figure 4. XRD patterns of synthesized TiO_2 NRs and semispherical NCs. Bragg peaks at 30.5°, 45.4°, 57.0°, 64.6°, 66.1°, and 74.6° indicate the existence of the anatase phase of TiO_2 (JCPDS No.01-086-1155) for NRs. XRD analyses clearly show the occurrence of other Bragg peaks at 34.6°, 35.9°, 52.7°, and 57.9° mainly due to semispherical NCs that are fit with the TiO_2(B) phase of titania with the reference card (JCPDS-00-046-1238). The (002), (−111), (003), and (020) reflections are typical of TiO_2(B) titania.

3.3. Liquid Crystalline Phases of TiO_2 NRs

In the next step, we investigate liquid crystal phases formed by the self-assembly of the anatase NRs made. As we showed in our early work elsewhere [18] that we are interested in the collective properties of TiO_2 NRs specifically for optical applications. We already showed that brookite TiO_2 NRs exhibit an intriguing LC phase behavior in bulk as well as promising switchability in external fields. Here, to compare anatase TiO_2 NRs with their brookite counterparts, we represent several self-assembled domains achieved on a carbon-coated copper TEM grid in the dry state as well as LC domains along with the sedimentation profile in a capillary in bulk (Figure 5). Similar to brookite TiO_2 NRs, anatase TiO_2 NRs can be fairly well approximated as spherocylinders with an effective aspect ratio (L/T) defined by the total length (L) divided by thickness (T). To obtain the relevant aspect ratio (AR) for self-assembly we also added 3.0 nm to both L and T, reflecting twice the effective length of the ligand molecules based on interparticle spacings measured from TEM images. The phase diagram for hard anisotropic shapes has been determined by Frenkel and Bolhuis using computer simulations [70]. However, colloidal rods are never all the same due to polydispersity in their length and diameter. Initially, Onsager predicted that length polydispersity in the system of hard rods broadens the biphasic region where longer rods preferentially enter the nematic phase [71]. Later, many papers investigated the effects of polydispersity for continuous distributions of rigid rods where they also found that increase in polydispersity shifts the isotropic boundary to lower concentrations while the nematic boundary moves to notably higher ones leading to a broadened biphasic region [39,72–76]. In our system, based on the average dimensions of the examined anatase NRs (L = 24.6 ± 3.4 nm and T = 3.6 ± 0.3 nm measured by TEM images), an effective aspect ratio of 4.2 was calculated which for monodisperse hard rods is close to the AR where next to nematic, also smectic LC phases can be formed and ABC-stacked crystals at high volume fractions [39,77,78]. Figure 5a depicts short smectic tracks of NRs aligned side-by-side in

several domains. For rods with hard interactions, it has been shown that smectic phases of hard rods nucleate first in 2D smectic layers which are most likely related to why such tracks form on top of a flat wall, but it should also be remembered that the drying forces are large compared to the average kinetic energy kT, where k is the Boltzmann's constant and T the absolute temperature. Therefore, it is also possible that these tracks are formed at the liquid–air interface, as it is known that being attached to the interface induces lateral forces between the rods because of the deformation of the interface [79].

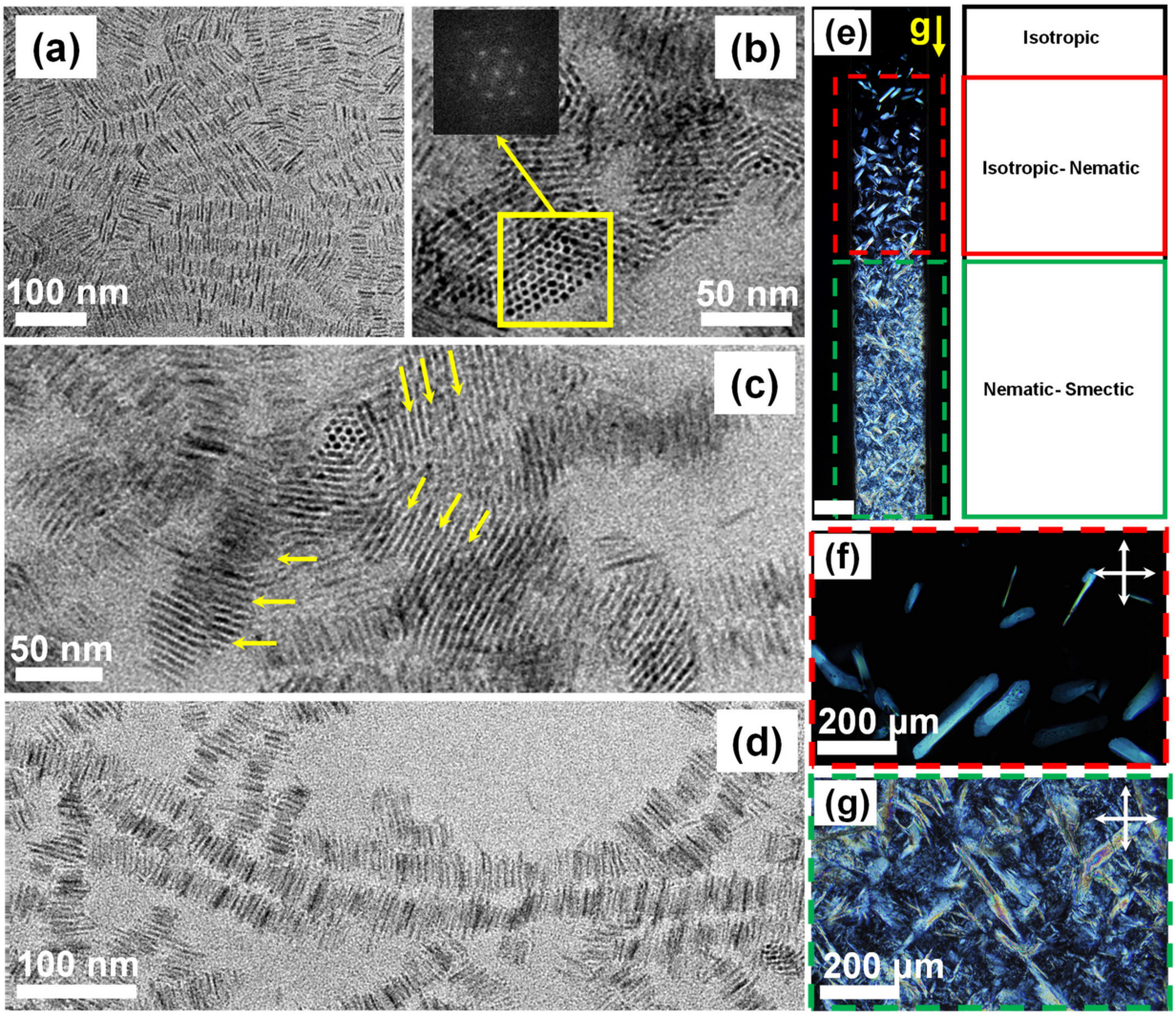

Figure 5. TEM micrographs of anatase NRs self-assembled on a TEM grid (**a**–**d**) and optical micrographs of a dispersion in toluene between crossed polarizers (**e**–**g**). (**a**) Anatase NRs in small smectic liquid crystal-like domains. (**b**,**c**) Hexagonal superlattices of vertically aligned anatase NRs. Inset in (**b**) shows the corresponding FFT pattern illustrating a close-packed hexagonal order. In (**c**), NRs have a tilted orientation, similar to rows of fallen dominoes (yellow arrows) around a vortex structure centered on a small cluster of locally homeotropically oriented NRs. In (**d**), a linear "rail-track" pattern was observed from the side-by-side assembly of the NRs into the rail-tracks of various lengths. (**e**) A sedimenting sample from a dispersion of anatase NRs in toluene (~29 vol%) in a capillary with three distinct regions. From top to bottom: isotropic fluid at the top, (**f**) elongated nematic tactoids floating in the isotropic fluid, and (**g**) coexistence of nematic domains and sharped-edge smectic LC phases. Scale bar in (**e**) is 500 µm.

Although the self-assembled arrays in Figure 5a seem to be a single layer, we presented some self-assembled domains in Figure 5b,c where part of the titania NRs were imaged

standing normal to the TEM grid evidencing more extended 2D smectic layer formation. The vertically aligned NR layers were seen to form with close-packed hexagonal order within the smectic layers (Figure 5b inset) [39]. Additionally, in some parts of the 2D smectic layers with the rods standing perpendicular most likely the drying forces made parts of the rods end up in a tilted orientation. Some of the rods fell over like dominoes in a certain direction; similar observations were made with different systems of NRs such as TiO_2 [18,80–82], CdS [83], CdSe [84], and CoO [85]. By considering the electron diffraction data, we conclude that these structures are otherwise the same as the vertically aligned arrays with a precise orientational and positional order and also the same interparticle separation as observed for the vertical superlattices. In Figure 5b,c we could also observe part of a vortex structure centered on one or a small cluster of locally homeotropically ordered rods. Since the orientation of the individual nanorods changed continuously around the vortex defect, it is similar to a disclination of strength +1 that can be observed in nematic liquid crystal phases [84,86]. The presence of this structure can be linked to twist or bend distortions of the nematic, and possibly also smectic liquid crystal domains produced by microflows during drying [87–89].

In Figure 5e–g, polarized optical microscopy (POM) images of the LC domains of anatase NRs are displayed. The initial volume fraction of these NRs was approximately 29 vol% and they were in an isotropic state showing no optical activity between cross polarizers. Analogous to our remarks in the previous report on brookite NRs lyotropic LCs [18], the dispersion of anatase NRs exhibited an equilibrium phase behavior along the concentration gradient that occurred in the capillary. Since these NRs were too small to sediment under gravity, this gradient was most likely formed by phase separation as a result of sufficiently high initial volume fraction and weak long-ranged van der Waals attractions. Along the capillary, three main regions were observed: the isotropic region on the top of the capillary, a biphasic region consisting of nematic tactoids nucleating and floating in the isotropic liquid, and a biphasic region of sharp-edged smectic domains in coexistence with a nematic at the bottom of the capillary that was quite identical to that of smectic-A LC phases of brookite NRs [18]. No striated LC texture indicative of a pure smectic phase was detected at the bottom of the capillary in the case of anatase NRs in comparison to brookite LCs. This could be attributed to the higher level of polydispersity in the length of the anatase NRs or the initial volume fraction could be too low to form such a phase. We also note that similar to the dispersion of brookite NRs reported elsewhere [18], a dispersion of anatase NRs in an isotropic state responded to an external electric field. An induced nematic LC phase was reversibly achieved known as a para nematic phase (results are not shown here). In our follow-up work in the near future, we intend to study these behaviors and dynamics in external electric fields.

As can be seen in Figure 5f,g, needle-like nematic tactoids nucleated in the isotropic liquid, and resulted in a biphasic region of sharp-edged smectic domains in coexistence with nematic domains. One should consider that tactoids are generally known to adopt a spindle shape depending on mesogen orientation, interfacial tensions, and elastic constants of the nematic phase [90,91]. Besides that, it has been shown that the existence of attractions among these colloidal mesogens in lyotropic LCs enhances this anisotropy toward needle-like tactoids [92–94]. In this regard, Green et al. [94] showed the phase behavior of rodlike particles with solvent-mediated attractions and repulsions. They showed that rods in the nematic tactoids are separated by average distances much smaller than their counterparts in the isotropic phase. Therefore, these rods in the nematic tactoid would spend considerably more time in the attractive well, which existed as a result of short-range electrostatic repulsive forces in combination with van der Waals attraction forces. Due to these attraction forces, the LC tactoids became needle-like and even in the case of highly attractive single-walled carbon nanotubes in superacids, they were referred to as "spaghetti" LC domains [94].

To roughly estimate the van der Waals attraction forces between the anatase cores and compare them with brookite counterparts, we calculate the van der Waals interactions

between anatase NRs and brookite NRs of the same size (solid and dashed lines, respectively in Figure 6) for three different relative orientations by using the Hamaker constants of anatase and brookite in toluene. The details of van der Waals interactions calculations have been described in detail in our earlier work [18]. As expected, the strongest attractions occur when rods are perfectly aligned face-to-face. However, the calculated interactions are an overestimation as they assume perfectly smooth inorganic cores with atomically flat interfaces. Any surface roughness and irregularities, as shown in HRTEM images in Figure 3, also would make the "perfect" parallel approach between the two rods much less efficient and reduce the actual van der Waals interactions [18,42]. The difference between anatase and brookite is seen to be very small. The vertical line at 3.0 nm shows the distance of the closest approach based on twice the ligand length. Therefore, both anatase and brookite NRs are expected to experience van der Waals attractions of a few *kT*, which may be sufficiently large to induce parallel alignment at high volume fractions, caused by their high refractive indexes. Nevertheless, employing apolar solvents with high refractive indexes in combination with the existence of atomic irregularities at the surface of NRs and sufficient steric repulsion between NRs by adsorbing ligand molecules could still efficiently reduce van der Waals attractions, making both of these material systems promising candidates for LC-based optical applications.

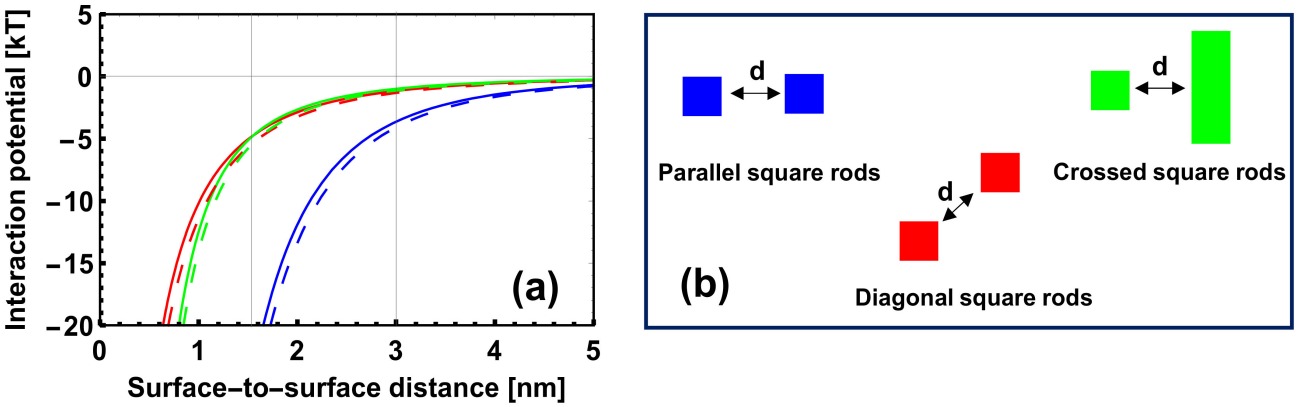

Figure 6. (**a**) van der Waals interaction potentials between two bare TiO_2 NRs of anatase (solid lines) and brookite (dashed lines) phase of the same size in toluene. Vertical gray solid lines represent one and two times the effective ligand length of 1.5 nm corresponding to the interparticle spacing observed in the TEM images. (**b**) Schematic representation of NRs encounter each other in parallel, diagonal, or crossed configuration shown in blue, red, and green colors, respectively. Nanorods are assumed as parallelepipeds of length 27.4 nm and thickness 3.4 nm.

4. Conclusions

In this work, we successfully synthesized highly crystalline organic-solvent-dispersible TiO_2 NRs based on a modified procedure from literature via a ligand-assisted nonhydrolytic sol-gel route. X-ray diffraction and selected area electron diffraction results showed the coexistence of anatase and TiO_2(B) phases of titania in the particles made. This synthesis yielded relatively concentrated dispersions of the anatase NRs (~500 mg/mL), after careful size-selective precipitation steps (yield of nearly 50%) to remove the largest rods as well as semispherical particles, which is twice the amount reported for the same size brookite NRs in ref. [18]. Possible reaction and formation mechanisms for the NRs were discussed based on the unusual observation that relatively early in the synthesis (after 10 min) rods were already present that subsequently reduced in length and increased in thickness during further growth, while semispherical particles were formed as well. Furthermore, we showed that anatase NRs were monodisperse enough to spontaneously self-assemble into smectic liquid crystalline phases on the TEM grid and in bulk. Because of their high refractive indexes and at the same time minimal light scattering due to their size,

both anatase and brookite TiO_2 dispersions are promising candidates for application in electro-optical devices based on inorganic liquid crystals.

Supplementary Materials: The following are available online at https://www.mdpi.com/article/10.3390/app12031614/s1. Figure S1: (a) A typical UV-Vis absorption spectrum of dilute dispersion of TiO_2 NRs in toluene. The spectrum shows a sharp absorption edge at 380 nm corresponding to band-to-band transitions. (b) Energy dependence of $(\alpha h\nu)^{0.5}$ versus photon energy $(h\nu)$ for the determination of the band gap derived from diffused UV-Vis absorption spectrum of TiO_2 NRs based on indirect transitions (n = 0.5) for anatase NRs. The bandgap of the anatase NRs was estimated based on ($\alpha = K(h\nu - E_g)^{0.5}/h\nu$) where E_g is the bandgap, α is the absorption coefficient, K is the absorption constant for indirect transitions, and $h\nu$ is the incident photon energy. The bandgap of the anatase NRs is equal to 3.28 eV which is calculated from the extrapolation of the absorption edge onto the energy axis where $\alpha = 0$. Table S1: Calculated parameters used in Scherrer equation ($L = K\lambda/\beta Cos\theta_\beta$), where ($\beta \cong 0.041b$), L is the average size, λ is the X-ray wavelength, β is the full-width at half maximum value calculated in radians by fitting peaks with a 4-parameter Gaussian profile, b is a coefficient in the 4-parameter Gaussian fit profile, θ_β is the Bragg angle for the measured peak, and K is a constant equal to 0.94.

Author Contributions: Conceptualization, S.N.H., A.v.B., A.I., P.J.B.; methodology and investigation, S.N.H.; HRTEM analysis, X.C.; writing—original draft preparation, S.N.H.; writing—review and editing, S.N.H., A.v.B., A.I., P.J.B.; supervision, A.I., P.J.B., A.v.B.; funding acquisition, A.v.B., A.I., P.J.B. All authors have read and agreed to the published version of the manuscript.

Funding: This research was funded by the Dutch Technology Foundation STW (grant 14176), which is part of the Netherlands Organization for Scientific Research- Applied and Engineering Sciences (NWO-TTW) and partly funded by the Ministry of Economic Affairs.

Institutional Review Board Statement: Not applicable.

Informed Consent Statement: Not applicable.

Data Availability Statement: Not applicable.

Acknowledgments: The authors acknowledge the Dutch Technology Foundation STW (grant 14176), which is part of the Netherlands Organization for Scientific Research-Applied and Engineering Sciences (NWO-TTW) and partly funded by the Ministry of Economic Affairs. X.C. acknowledges the European Research Council for their support via the ERC Consolidator Grant NANO-INSITU (grant 683076). The authors would like to thank Dennie Wezendonk for the X-ray measurements, Peter Helfferich for his help during POM measurements, Chris Schneijdenberg for technical assistance in electron microscopy analysis, Albert Grau-Carbonell for carrying out numerical calculations for van der Waals interaction potentials, and Dagney Mackaaij for her contributions on titania synthesis experiments.

Conflicts of Interest: The authors declare no conflict of interest.

References

1. Bai, Y.; Mora-Sero, I.; De Angelis, F.; Bisquert, J.; Wang, P. Titanium dioxide nanomaterials for photovoltaic applications. *Chem. Rev.* **2014**, *114*, 10095–10130. [CrossRef]
2. Magalhães, P.; Andrade, L.; Nunes, O.C.; Mendes, A. Titanium dioxide photocatalysis: Fundamentals and application on photoinactivation. *Rev. Adv. Mater. Sci.* **2017**, *51*, 91–129.
3. Cargnello, M.; Montini, T.; Smolin, S.Y.; Priebe, J.B.; Delgado Jaén, J.J.; Doan-Nguyen, V.V.T.; McKay, I.S.; Schwalbe, J.A.; Pohl, M.-M.; Gordon, T.R.; et al. Engineering titania nanostructure to tune and improve its photocatalytic activity. *Proc. Natl. Acad. Sci. USA* **2016**, *113*, 3966–3971. [CrossRef]
4. Bourikas, K.; Kordulis, C.; Lycourghiotis, A. Titanium dioxide (Anatase and Rutile): Surface chemistry, liquid-solid interface chemistry, and scientific synthesis of supported catalysts. *Chem. Rev.* **2014**, *114*, 9754–9823. [CrossRef] [PubMed]
5. Gordon, T.R.; Cargnello, M.; Paik, T.; Mangolini, F.; Weber, R.T.; Fornasiero, P.; Murray, C.B. Nonaqueous synthesis of TiO_2 nanocrystals using TiF4 to engineer morphology, oxygen vacancy concentration, and photocatalytic activity. *J. Am. Chem. Soc.* **2012**, *134*, 6751–6761. [CrossRef] [PubMed]
6. Casavola, M.; Buonsanti, R.; Caputo, G.; Cozzoli, P.D. Colloidal strategies for preparing oxide-based hybrid nanocrystals. *Eur. J. Inorg. Chem.* **2008**, 837–854. [CrossRef]

7. Katal, R.; Masudy-Panah, S.; Tanhaei, M.; Farahani, M.H.D.A.; Jiangyong, H. A review on the synthesis of the various types of anatase TiO_2 facets and their applications for photocatalysis. *Chem. Eng. J.* **2020**, *384*, 123384. [CrossRef]
8. Zhang, H.; Banfield, J.F. Structural characteristics and mechanical and thermodynamic properties of nanocrystalline TiO_2. *Chem. Rev.* **2014**, *114*, 9613–9644. [CrossRef] [PubMed]
9. Ma, Y.; Wang, X.L.; Jia, Y.S.; Chen, X.B.; Han, H.X.; Li, C. Titanium Dioxide-Based Nanomaterials for Photocatalytic Fuel Generations. *Chem. Rev.* **2014**, *114*, 9987–10043. [CrossRef]
10. Bai, J.; Zhou, B. Titanium Dioxide Nanomaterials for Sensor Applications. *Chem. Rev.* **2014**, *114*, 10131–10176. [CrossRef]
11. Kern, P.; Schwaller, P.; Michler, J. Electrolytic deposition of titania films as interference coatings on biomedical implants: Microstructure, chemistry and nano-mechanical properties. *Thin Solid Films* **2006**, *494*, 279–286. [CrossRef]
12. Sungur, Ş. Titanium Dioxide Nanoparticles. In *Handbook of Nanomaterials and Nanocomposites for Energy and Environmental Applications*; Springer: Cham, Switzerland, 2021; pp. 713–730, ISBN 978-3-030-36268-3.
13. Zhang, H.; Banfield, J.F. Thermodynamic analysis of phase stability of nanocrystalline titania. *J. Mater. Chem.* **1998**, *8*, 2073–2076. [CrossRef]
14. Ranade, M.R.; Navrotsky, A.; Zhang, H.Z.; Banfield, J.F.; Elder, S.H.; Zaban, A.; Borse, P.H.; Kulkarni, S.K.; Doran, G.S.; Whitfield, H.J. Energetics of nanocrystalline TiO_2. *Proc. Natl. Acad. Sci. USA* **2002**, *99*, 6476–6481. [CrossRef] [PubMed]
15. Zhang, H.; Banfield, J.F. Understanding polymorphic phase transformation behavior during growth of nanocrystalline aggregates: Insights from TiO_2. *J. Phys. Chem. B* **2000**, *104*, 3481–3487. [CrossRef]
16. Mason, C.W.; Yeo, I.; Saravanan, K.; Balaya, P. Interconnected nanofibrous titanium dioxide bronze: An emerging lithium ion anode material for high rate performance. *RSC Adv.* **2013**, *3*, 2935–2941. [CrossRef]
17. Voepel, P.; Seitz, C.; Waack, J.M.; Zahn, S.; Leichtweiß, T.; Zaichenko, A.; Mollenhauer, D.; Amenitsch, H.; Voggenreiter, M.; Polarz, S.; et al. Peering into the mechanism of low-temperature synthesis of bronze-type TiO_2 in ionic liquids. *Cryst. Growth Des.* **2017**, *17*, 5586–5601. [CrossRef]
18. Hosseini, S.N.; Grau-Carbonell, A.; Nikolaenkova, A.G.; Xie, X.; Chen, X.; Imhof, A.; van Blaaderen, A.; Baesjou, P.J. Smectic Liquid Crystalline Titanium Dioxide Nanorods: Reducing Attractions by Optimizing Ligand Density. *Adv. Funct. Mater.* **2020**, *30*, 1–11. [CrossRef]
19. Park, S.; Mundoor, H.; Fleury, B.; Davidson, P.; van de Lagemaat, J.; Smalyukh, I.I. Liquid Crystalline Order and Electric Switching of Upconversion Luminescence in Colloidal Nanorod Suspensions. *Adv. Opt. Mater.* **2019**, *7*, 1–8. [CrossRef]
20. Cozzoli, P.D.; Kornowski, A.; Weller, H. Low-Temperature Synthesis of Soluble and Low-Temperature Synthesis of Soluble and Processable. *J. Am. Chem. Soc.* **2003**, *125*, 14539–14548. [CrossRef]
21. Lee, K.; Mazare, A.; Schmuki, P. One-dimensional titanium dioxide nanomaterials: Nanotubes. *Chem. Rev.* **2014**, *114*, 9385–9454. [CrossRef]
22. Cargnello, M.; Gordon, T.R.; Murray, C.B. Solution-Phase Synthesis of Titanium Dioxide Nanoparticles and Nanocrystals. *Chem. Rev.* **2014**, *114*, 9319–9345. [CrossRef] [PubMed]
23. Gabriel, J.C.P.; Davidson, P. New trends in colloidal liquid crystals based on mineral moieties. *Adv. Mater.* **2000**, *12*, 9–20. [CrossRef]
24. Sonin, A.S. Inorganic lyotropic liquid crystals. *J. Mater. Chem.* **1998**, *8*, 2557–2574. [CrossRef]
25. Trentler, T.J.; Denler, T.E.; Bertone, J.F.; Agrawal, A.; Colvin, V.L. Synthesis of TiO_2 nanocrystals by nonhydrolytic solution-based reactions. *J. Am. Chem. Soc.* **1999**, *121*, 1613–1614. [CrossRef]
26. Chemseddine, A.; Moritz, T. Nanostructuring titania: Control over nanocrystal structure, size, shape, and organization. *Eur. J. Inorg. Chem.* **1999**, 235–245. [CrossRef]
27. Jun, Y.W.; Casula, M.F.; Sim, J.H.; Kim, S.Y.; Cheon, J.; Alivisatos, A.P. Surfactant-Assisted Elimination of a High Energy Facet as a Means of Controlling the Shapes of TiO_2 Nanocrystals. *J. Am. Chem. Soc.* **2003**, *125*, 15981–15985. [CrossRef]
28. Niederberger, M.; Bartl, M.H.; Stucky, G.D. Benzyl alcohol and titanium tetrachloride - A versatile reaction system for the nonaqueous and low-temperature preparation of crystalline and luminescent titania nanoparticles. *Chem. Mater.* **2002**, *14*, 4364–4370. [CrossRef]
29. Arnal, P.; Corriu, R.J.P.; Leclercq, D.; Mutin, P.H.; Vioux, A. A Solution Chemistry Study of Nonhydrolytic Sol - Gel Routes to Titania. *Chem. Mater.* **1997**, *9*, 694–698. [CrossRef]
30. Mutin, P.H.; Vioux, A. Nonhydrolytic processing of oxide-based materials: Simple routes to control homogeneity, morphology, and nanostructure. *Chem. Mater.* **2009**, *21*, 582–596. [CrossRef]
31. Zhang, Z.; Zhong, X.; Liu, S.; Li, D.; Han, M. Aminolysis route to monodisperse titania nanorods with tunable aspect ratio. *Angew. Chem. Int. Ed.* **2005**, *44*, 3466–3470. [CrossRef]
32. Buonsanti, R.; Grillo, V.; Carlino, E.; Giannini, C.; Kipp, T.; Cingolani, R.; Cozzoli, P.D. Nonhydrolytic synthesis of high-quality anisotropically shaped brookite TiO_2 nanocrystals. *J. Am. Chem. Soc.* **2008**, *130*, 11223–11233. [CrossRef]
33. Buonsanti, R.; Carlino, E.; Giannini, C.; Altamura, D.; De Marco, L.; Giannuzzi, R.; Manca, M.; Gigli, G.; Cozzoli, P.D. Hyperbranched Anatase TiO_2 Nanocrystals: Nonaqueous Synthesis, Growth Mechanism, and Exploitation in Dye-Sensitized Solar Cells. *J. Am. Chem. Soc.* **2011**, *133*, 19216–19239. [CrossRef] [PubMed]
34. Joo, J.; Kwon, S.G.; Yu, T.; Cho, M.; Lee, J.; Yoon, J. Large-Scale Synthesis of TiO_2 Nanorods via Nonhydrolytic Sol-Gel Ester Elimination Reaction and Their Application to Photocatalytic Inactivation of E. coli. *J. Phys. Chem. B* **2005**, 15297–15302. [CrossRef] [PubMed]

35. Koo, B.; Park, J.; Kim, Y.; Choi, S.H.; Sung, Y.E.; Hyeon, T. Simultaneous phase- and size-controlled synthesis of TiO_2 nanorods via non-hydrolytic sol-gel reaction of syringe pump delivered precursors. *J. Phys. Chem. B* **2006**, *110*, 24318–24323. [CrossRef] [PubMed]
36. Levy, D.; Marcos, Z. *The Sol-Gel Handbook*; Levy, D., Marcos, Z., Eds.; Wiley-VCH: Weinheim, Germany, 2015; ISBN 9783527338443.
37. Kobayashi, M.; Saito, H.; Boury, B.; Matsukawa, K.; Sugahara, Y. Epoxy-based hybrids using TiO_2 nanoparticles prepared via a non-hydrolytic sol-gel route. *Appl. Organomet. Chem.* **2013**, *27*, 673–677. [CrossRef]
38. Lee, B.; Littrell, K.; Sha, Y.; Shevchenko, E.V. Revealing the Effects of the Non-solvent on the Ligand Shell of Nanoparticles and Their Crystallization. *J. Am. Chem. Soc.* **2019**, *141*, 16651–16662. [CrossRef]
39. Kuijk, A.; Byelov, D.V.; Petukhov, A.V.; van Blaaderen, A.; Imhof, A. Phase behavior of colloidal silica rods. *Faraday Discuss.* **2012**, *159*, 181–199. [CrossRef]
40. Niederberger, M.; Pinna, N. *Metal Oxide Nanoparticles in Organic Solvents: Synthesis, Formation, Assembly and Application*; Springer: London, UK, 2009; ISBN 9781848826700.
41. Murray, C.B.; Kagan, C.R.; Bawendi, M.G. Synthesis And Characterization Of Monodisperse Nanocrystals And Close-Packed Nanocrystal Assemblies. *Annu. Rev. Mater. Sci.* **2000**, *30*, 545–610. [CrossRef]
42. Israelachvili, J.N. *Intermolecular and Surface Forces*, 3rd ed.; Elsevier: Amsterdam, The Netherlands, 2011; ISBN 9780123919274.
43. Penn, R.L.; Banfield, J.F. Morphology development and crystal growth in nanocrystalline aggregates under hydrothermal conditions: Insights from titania. *Geochim. Cosmochim. Acta* **1999**, *63*, 1549–1557. [CrossRef]
44. Niederberger, M.; Garnweitner, G.; Pinna, N.; Neri, G. Non-aqueous routes to crystalline metal oxide nanoparticles: Formation mechanisms and applications. *Prog. Solid State Chem.* **2005**, *33*, 59–70. [CrossRef]
45. Niederberger, M. Nonaqueous Sol – Gel Routes to Metal Oxide Nanoparticles. *Acc. Chem. Res.* **2007**, *40*, 793–800. [CrossRef] [PubMed]
46. Deshmukh, R.; Niederberger, M. Nonhydrolytic Sol – Gel Methods. In *The Sol–Gel Handbook: Synthesis, Characterization, and Applications*; Wiley-VCH: Weinheim, Germany, 2015; pp. 29–69.
47. Dalmaschio, C.J.; Leite, E.R. Detachment induced by rayleigh-instability in metal oxide nanorods: Insights from TiO_2. *Cryst. Growth Des.* **2012**, *12*, 3668–3674. [CrossRef]
48. Niederberger, M.; Bartl, M.H.; Stucky, G.D. Benzyl alcohol and transition metal chlorides as a versatile reaction system for the nonaqueous and low-temperature synthesis of crystalline nano-objects with controlled dimensionality. *J. Am. Chem. Soc.* **2002**, *124*, 13642–13643. [CrossRef] [PubMed]
49. Li, X.L.; Peng, Q.; Yi, J.X.; Wang, X.; Li, Y. Near monodisperse TiO_2 nanoparticles and nanorods. *Chem. A Eur. J.* **2006**, *12*, 2383–2391. [CrossRef] [PubMed]
50. Jiang, D.; Xu, Y.; Hou, B.; Wu, D.; Sun, Y. A simple non-aqueous route to anatase TiO_2. *Eur. J. Inorg. Chem.* **2008**, 1236–1240. [CrossRef]
51. Zhu, J.; Zhang, J.; Chen, F.; Anpo, M. Preparation of high photocatalytic activity TiO_2 with a bicrystalline phase containing anatase and TiO_2 (B). *Mater. Lett.* **2005**, *59*, 3378–3381. [CrossRef]
52. Cargnello, M.; Cargnello, M.; Doan-nguyen, V.V.T.; Gordon, T.R.; Diaz, R.E.; Stach, E.A.; Gorte, R.J.; Fornasiero, P.; Murray, C.B. Control of Metal Nanocrystal Size Role for Ceria Catalysts. *Science* **2014**, *771*, 771–774. [CrossRef]
53. Casavola, M.; Grillo, V.; Carlino, E.; Giannini, C.; Gozzo, F.; Pinel, E.F.; Garcia, M.A.; Manna, L.; Cingolani, R.; Cozzoli, P.D. Topologically controlled growth of magnetic-metal-functionalized semiconductor oxide nanorods. *Nano Lett.* **2007**, *7*, 1386–1395. [CrossRef]
54. Barnard, A.S.; Curtiss, L.A. Prediction of TiO_2 nanoparticle phase and shape transitions controlled by surface chemistry. *Nano Lett.* **2005**, *5*, 1261–1266. [CrossRef] [PubMed]
55. Da Silva, R.O.; Gonalves, R.H.; Stroppa, D.G.; Ramirez, A.J.; Leite, E.R. Synthesis of recrystallized anatase TiO_2 mesocrystals with Wulff shape assisted by oriented attachment. *Nanoscale* **2011**, *3*, 1910–1916. [CrossRef]
56. Dalmaschio, C.J.; Ribeiro, C.; Leite, E.R. Impact of the colloidal state on the oriented attachment growth mechanism. *Nanoscale* **2010**, *2*, 2336–2345. [CrossRef]
57. Zhang, J.; Huang, F.; Lin, Z. Progress of nanocrystalline growth kinetics based on oriented attachment. *Nanoscale* **2010**, *2*, 18–34. [CrossRef]
58. Nichols, F.A.; Mullins, W.W. Contributions to Morphological Changes Driven by Capillarity. *Trans. Met. Soc. AIME* **1965**, *233*.
59. Karim, S.; Toimil-Molares, M.E.; Ensinger, W.; Balogh, A.G.; Cornelius, T.W.; Khan, E.U.; Neumann, R. Influence of crystallinity on the Rayleigh instability of gold nanowires. *J. Phys. D. Appl. Phys.* **2007**, *40*, 3767–3770. [CrossRef]
60. Qin, Y.; Lee, S.M.; Pan, A.; Gösele, U.; Knez, M. Rayleigh-instability-induced metal nanoparticle chains encapsulated in nanotubes produced by atomic layer deposition. *Nano Lett.* **2008**, *8*, 114–118. [CrossRef] [PubMed]
61. Qin, Y.; Liu, L.; Yang, R.; Gösele, U.; Knez, M. General assembly method for linear metal nanoparticle chains embedded in nanotubes. *Nano Lett.* **2008**, *8*, 3221–3225. [CrossRef]
62. Dinh, C.; Nguyen, T.; Kleitz, F.; Do, T. Shape-Controlled Synthesis of Highly Crystalline Titania Nanocrystals. *ACS Nano* **2009**, *3*, 3737–3743. [CrossRef] [PubMed]
63. Penn Lee, R.; Banfield, F.J. Formation of rutile nuclei at anatase (112) twin interfaces and the phase transformation mechanism in nanocrystalline titania. *Am. Mineral.* **1999**, *84*, 871–876. [CrossRef]

64. Reddy, K.M.; Manorama, S.V.; Reddy, A.R. Bandgap studies on anatase titanium dioxide nanoparticles. *Mater. Chem. Phys.* **2003**, *78*, 239–245. [CrossRef]
65. Holzwarth, U.; Gibson, N. The Scherrer equation versus the "Debye-Scherrer equation". *Nat. Nanotechnol.* **2011**, *6*, 534. [CrossRef]
66. Gonzalo-Juan, I.; McBride, J.R.; Dickerson, J.H. Ligand-mediated shape control in the solvothermal synthesis of titanium dioxide nanospheres, nanorods and nanowires. *Nanoscale* **2011**, *3*, 3799–3804. [CrossRef] [PubMed]
67. Kandiel, T.A.; Feldhoff, A.; Robben, L.; Dillert, R.; Bahnemann, D.W. Tailored titanium dioxide nanomaterials: Anatase nanoparticles and brookite nanorods as highly active photocatalysts. *Chem. Mater.* **2010**, *22*, 2050–2060. [CrossRef]
68. Li, J.G.; Ishigaki, T.; Sun, X. Anatase, brookite, and rutile nanocrystals via redox reactions under mild hydrothermal conditions: Phase-selective synthesis and physicochemical properties. *J. Phys. Chem. C* **2007**, *111*, 4969–4976. [CrossRef]
69. Andreev, Y.G.; Panchmatia, P.M.; Liu, Z.; Parker, S.C.; Islam, M.S.; Bruce, P.G. The shape of TiO_2-B nanoparticles. *J. Am. Chem. Soc.* **2014**, *136*, 6306–6312. [CrossRef] [PubMed]
70. Bolhuis, P.; Frenkel, D. Tracing the phase boundaries of hard spherocylinders. *J. Chem. Phys.* **1997**, *106*, 666–687. [CrossRef]
71. Onsager, L. The Effects of Shape on the Interaction of Colloidal Particles. *Ann. N. Y. Acad. Sci.* **1949**, *51*, 627–659. [CrossRef]
72. Buining, P.A.; Lekkerkerker, H.N.W. Isotropic-Nematic Phase Separation of Dispersion of Organophilic Boehmite Rods D/L. *J. Phys. Chem.* **1993**, *97*, 11510–11516. [CrossRef]
73. Bohle, A.M.; Hołyst, R.; Vilgis, T. Polydispersity and Ordered Phases in Solutions of Rodlike Macromolecules. *Phys. Rev. Lett.* **1996**, *76*, 1396–1399. [CrossRef]
74. Van Bruggen, M.P.B.; Dhont, J.K.G.; Lekkerkerker, H.N.W. Morphology and kinetics of the isotropic-nematic phase transition in dispersions of hard rods. *Macromolecules* **1999**, *32*, 2256–2264. [CrossRef]
75. Vroege, G.J.; Petukhov, A.V.; Lemaire, B.J.; Davidson, P. Smectic liquid-crystalline order in suspensions of highly polydisperse goethite nanorods. *Adv. Mater.* **2006**, *18*, 2565–2568. [CrossRef]
76. Wensink, H.H.; Vroege, G.J. Isotropic – nematic phase behavior of length- polydisperse hard rods. *J. Chem. Phys.* **2003**, *119*, 6868–6882. [CrossRef]
77. Savenko, S.V.; Dijkstra, M. Sedimentation and multiphase equilibria in suspensions of colloidal hard rods. *Phys. Rev. E* **2004**, *70*, 51401. [CrossRef] [PubMed]
78. Savenko, S.V.; Dijkstra, M. Phase behavior of a suspension of colloidal hard rods and nonadsorbing polymer. *J. Chem. Phys.* **2006**, *124*. [CrossRef] [PubMed]
79. Pietra, F.; Rabouw, F.T.; Evers, W.H.; Byelov, D.V.; Petukhov, A.V.; De Mello Donegá, C.; Vanmaekelbergh, D. Semiconductor nanorod self-assembly at the liquid/air interface studied by in situ GISAXS and ex situ TEM. *Nano Lett.* **2012**, *12*, 5515–5523. [CrossRef] [PubMed]
80. Ye, B.; Qian, G.; Fan, X.; Wang, Z. Self-Assembled Superlattices from Colloidal TiO 2 Nanorods. *Curr. Nanosci.* **2010**, *6*, 262–268. [CrossRef]
81. Ren, Z.; Chen, C.; Hu, R.; Mai, K.; Qian, G.; Wang, Z. Two-step self-assembly and lyotropic liquid crystal behavior of TiO_2 nanorods. *J. Nanomater.* **2012**, *2012*, 180989. [CrossRef]
82. Zhang, Y.; Liu, F.M. Large-scale superlattices from colloidal TiO_2nanorods: A facile self-assembly approach. *Appl. Surf. Sci.* **2016**, *367*, 559–562. [CrossRef]
83. Ryan, K.M.; Mastroianni, A.; Stancil, K.A.; Liu, H.; Alivisatos, A.P. Electric-field-assisted assembly of perpendicularly oriented nanorod superlattices. *Nano Lett.* **2006**, *6*, 1479–1482. [CrossRef]
84. Li, L.S.; Alivisatos, A.P. Semiconductor nanorod liquid crystals and their assembly on a substrate. *Adv. Mater.* **2003**, *15*, 408–411. [CrossRef]
85. An, K.; Lee, N.; Park, J.; Kim, S.C.; Hwang, Y.; Park, J.G.; Kim, J.Y.; Park, J.H.; Han, M.J.; Yu, J.; et al. Synthesis, characterization, and self-assembly of pencil-shaped CoO nanorods. *J. Am. Chem. Soc.* **2006**, *128*, 9753–9760. [CrossRef] [PubMed]
86. Kim, F.; Kwan, S.; Akana, J.; Yang, P. Langmuir-Blodgett nanorod assembly. *J. Am. Chem. Soc.* **2001**, *123*, 4360–4361. [CrossRef] [PubMed]
87. Diroll, B.T.; Greybush, N.J.; Kagan, C.R.; Murray, C.B. Smectic nanorod superlattices assembled on liquid subphases: Structure, orientation, defects, and optical polarization. *Chem. Mater.* **2015**, *27*, 2998–3008. [CrossRef]
88. Xie, Y.; Liang, Y.; Chen, D.; Wu, X.; Dai, L.; Liu, Q. Vortical superlattices in a gold nanorods' self-assembled monolayer. *Nanoscale* **2014**, *6*, 3064–3068. [CrossRef] [PubMed]
89. Querner, C.; Fischbein, M.D.; Heiney, P.A.; Drndić, M. Millimeter-scale assembly of CdSe nanorods into smectic superstructures by solvent drying kinetics. *Adv. Mater.* **2008**, *20*, 2308–2314. [CrossRef]
90. Modlinska, A.; Alsayed, A.M.; Gibaud, T. Condensation and dissolution of nematic droplets in dispersions of colloidal rods with thermo-sensitive depletants. *Sci. Rep.* **2015**, *5*, 1–10. [CrossRef]
91. Prinsen, P.; van der Schoot, P. Shape and director-field transformation of tactoids. *Phys. Rev. E* **2003**, *68*, 11. [CrossRef] [PubMed]
92. Wang, P.; MacLachlan, M.J. Liquid crystalline tactoids: Ordered structure, defective coalescence and evolution in confined geometries. *Philos. Trans. R. Soc. A Math. Phys. Eng. Sci.* **2018**, *376*, 20170042. [CrossRef] [PubMed]
93. Jamali, V.; Behabtu, N.; Senyuk, B.; Lee, J.A.; Smalyukh, I.I.; van Der Schoot, P.; Pasquali, M. Experimental realization of crossover in shape and director field of nematic tactoids. *Phys. Rev. E Stat. Nonlinear Soft Matter Phys.* **2015**, *91*, 1–7. [CrossRef]
94. Green, M.J.; Parra-Vasquez, A.N.G.; Behabtu, N.; Pasquali, M. Modeling the phase behavior of polydisperse rigid rods with attractive interactions with applications to single-walled carbon nanotubes in superacids. *J. Chem. Phys.* **2009**, 131. [CrossRef]